

Review

Phosphors and Scintillators in Biomedical Imaging

Christos Michail , Panagiotis Liaparinos , Nektarios Kalyvas , Ioannis Kandarakis *, George Fountos and Ioannis Valais 

Radiation Physics, Materials Technology and Biomedical Imaging Laboratory, Department of Biomedical Engineering, University of West Attica, Ag. Spyridonos, 12210 Athens, Greece; cmichail@uniwa.gr (C.M.); liapkin@uniwa.gr (P.L.); nkalyvas@uniwa.gr (N.K.); gfoun@uniwa.gr (G.F.); valais@uniwa.gr (I.V.)

* Correspondence: kandarakis@uniwa.gr

Abstract: Medical imaging instrumentation is mostly based on the use of luminescent materials coupled to optical sensors. These materials are employed in the form of granular screens, structured crystals, single transparent crystals, ceramics, etc. Storage phosphors are also incorporated in particular X-ray imaging systems. The physical properties of these materials should match the criteria required by the detective systems employed in morphological and functional biomedical imaging. The systems are analyzed based on theoretical frameworks emanating from the linear cascaded systems theory as well as the signal detection theory. Optical diffusion has been studied by different methodological approaches, such as experimental measurements and analytical modeling, including geometrical optics and Monte Carlo simulation. Analysis of detector imaging performance is based on image quality metrics, such as the luminescence emission efficiency (LE), the modulation transfer function (MTF), the noise power spectrum (NPS), and the detective quantum efficiency (DQE). Scintillators and phosphors may present total energy conversion on the order of 0.001–0.013 with corresponding DQE in the range of 0.1–0.6. Thus, the signal-to-noise ratio, which is crucial for medical diagnosis, shows clearly higher values than those of the energy conversion.

Keywords: scintillators; single crystals; phosphors; radiation detectors; medical imaging; image quality



Citation: Michail, C.; Liaparinos, P.; Kalyvas, N.; Kandarakis, I.; Fountos, G.; Valais, I. Phosphors and Scintillators in Biomedical Imaging. *Crystals* **2024**, *14*, 169. <https://doi.org/10.3390/cryst14020169>

Academic Editors: Yutaka Fujimoto and Ana M. Garcia-Deibe

Received: 8 January 2024

Revised: 26 January 2024

Accepted: 3 February 2024

Published: 7 February 2024



Copyright: © 2024 by the authors. Licensee MDPI, Basel, Switzerland. This article is an open access article distributed under the terms and conditions of the Creative Commons Attribution (CC BY) license (<https://creativecommons.org/licenses/by/4.0/>).

1. Background

Over the past thirty years, several featured review articles have been published either providing the fundamental physical and scintillating properties of several phosphor materials or describing the practical importance of such materials in detective medical imaging systems [1–16]. We considered it important to extend these reviews of the literature by providing up-to-date information on phosphor material research in combination with medical image science.

Medical imaging systems follow various classifications depending on their physical principle, mode of operation, and medical use. Firstly, the systems are classified into those using *ionizing radiations*, i.e., X-rays or radioactive sources (diagnostic radiology, nuclear medicine, portal imaging), and those using *non-ionizing phenomena*, i.e., nuclear magnetic resonance (NMR), reflection and scattering of ultrasonic waves, etc. Considering purely medical applications, imaging methods are divided into: (i) *morphological imaging*, highlighting shape, dimensions, and coordinates of anatomical structures as well as mechanical movement, the flow of biological fluids, i.e., in cardiovascular mechanisms, etc., and (ii) *functional imaging*, highlighting mechanisms of biological character including processes at the molecular level. The techniques of imaging follow two basic directions: (i) *projection imaging*, where anatomical structures are projected onto a two-dimensional detecting area and (ii) *tomographic imaging*, where images of anatomic cross-sections are mathematically reconstructed from data obtained by measurements taken peripherally on the human body. For both of the aforementioned cases, measurement techniques may

be also divided into *transmission* and *emission* modes. In transmission mode, radiation, emitted from a source outside the human body, passes through it before impinging at the detector surface, while in emission mode, radiation is emitted by a radioactive substance administered inside the body to follow particular functions of a biological nature [6,17–27].

A final classification of medical imaging detectors is related to their use in medicine. The main areas of medical imaging are *diagnostic radiology* (morphological imaging based on X-rays) and *nuclear medicine* (functional imaging based on radioactivity). Portal imaging systems, incorporated in *radiation therapy* machines, are based on similar principles of operation as those of diagnostic radiology. X-ray screen-film radiography (SFR), digital radiography (DR) and fluoroscopy (DF), full field mammography (FFDM), computed radiography (CR), and X-ray computed tomography (CT) constitute the main equipment found in diagnostic radiology departments, while gamma camera single-photon emission computed tomography (SPECT) and positron emission tomography (PET) are systems belonging to nuclear medicine. To a large extent, medical imaging technology is based on radiation detectors using scintillators and phosphors combined with optical sensors of various technologies. These include large-area hydrogenated amorphous silicon (a-Si:H) active-matrix photodiode arrays (AMFPDs), complementary metal oxide semiconductors (CMOSs), charge-coupled devices (CCDs) photomultiplier tubes (PMTs), avalanche photodiodes (APDs), and silicon multipliers (SiPMs) (for detection of radioactivity photons). Radiation detectors based on luminescence are often referred to as *indirect conversion* imaging systems, while detectors using photoconductors (e.g., amorphous selenium) or semiconductors (e.g., cadmium telluride) are characterized as *direct conversion* systems [17,19–23,28,29]. Furthermore, detectors are also categorized into (i) *energy-integrating devices* and (ii) *photon-counting devices*. Energy integration detectors produce an output signal determined by the total energy absorbed [22,23,28,30]. In the case of photon counting, a series of pulses is produced one by one, corresponding to the measured incident photons [4–6,17,18,31,32].

Energy integrating systems are principally employed in diagnostic radiology and radiation therapy (i.e., in portal imaging detectors) [22,33]. In nuclear medicine, detectors are photon-counting devices that perform gamma-ray spectrometry, i.e., they measure incoming photons one by one and produce a series of corresponding pulses [20]. These pulses are then classified according to their amplitude (proportional to photon energy) by a pulse height analyzer to produce a gamma-ray spectrum. These systems are based on single-crystal scintillators coupled to conventional PMTs, position-sensitive devices (PSPMT), APD arrays, or SiPMs. In special cases, suitably designed counters are also employed in radiology [34].

2. Use of Scintillators and Phosphors in Medical Imaging

Scintillators and phosphors are materials that emit fluorescence photons after the absorption of ionizing radiation [4–6,31,32,35]. In inorganic materials, the absorption of a radiation photon liberates a fast electron (e.g., photoelectron, etc.), which moves through the material and transfers energy to the electrons of the lattice. The electrons are subsequently excited and enter the conduction band. Each fast electron creates a large number of conduction electron–hole pairs. Electrons from electron–hole pairs move freely within the lattice until they arrive at a luminescence center (ion activator creating energy levels within the forbidden bandgap of the material) and go into one of its excited energy levels. The holes are also displaced from their original position and are collected at points where the activators are located. If the transition from the excited to the ground energy level of the activator is allowed, then the electron is de-excited to the ground level and recombines with the hole. This is a de-excitation process that can cause the emission of a fluorescent photon. The whole process has two inherent drawbacks related to the liberation of fast electrons. First, the range of these electrons may be long enough (e.g., 20–30 μm) to result in a difference between the point of radiation incidence and the point of luminescence creation. This reduces the accuracy of projection imaging and spatial

resolution. Second, the emission of K-fluorescence X-ray photons just after the liberation of the fast electron [17,19]. These photons may re-interact at a point different from the initial interaction, hence creating a second point of fluorescence emission. In organic compounds, the luminescence mechanism results from molecular excitation after the absorption of the radiation photon, and then a de-excitation occurs. It is principally determined by the molecule structure and not by the crystal lattice structure [16].

Scintillators are employed under various configurations including the following:

- (a) Thin screens (approximately 150–300 μm thick) containing phosphor grains of various sizes (in the range from nano to some micrometers) manufactured in large areas (e.g., $18 \times 24 \text{ cm}^2$, $35 \times 43 \text{ cm}^2$, etc.), which are employed in traditional X-ray projection imaging as energy-integrating detectors, morphological imaging including X-ray screen-film radiography, active matrix flat panel arrays in digital radiography and fluoroscopy, and portal imaging (therapeutic imaging). Materials in this form are often referred to as *phosphors*, although the term *scintillating screen* has also been used. In this type of large-area detector, light spread within the material's mass is deleterious for accurate position determination and image quality. Grains limit lateral spread effects by scattering and attenuating the laterally directed light photons. Grain size and shape affect both the emission efficiency and the imaging performance of the whole imaging system, i.e., small grains improve spatial resolution, while larger grains ameliorate screen sensitivity. An additional factor required to take into account is the thickness of the particular screen. Thick screens absorb larger fractions of incident radiation, while thin screens improve spatial resolution. Traditionally, rare earth phosphors (e.g., $\text{Gd}_2\text{O}_2\text{S:Tb}$) are the most popular for such applications, although many new materials are actually investigated. Detectors in digital radiography and mammography may contain large numbers of optical sensor elements (e.g., up to 4288×4288 photodiode arrays with pixel pitch between 50 and 200 μm , or even 20 μm with CMOS technology, covered by a large-area phosphor screen). The drawbacks of projection X-ray imaging, creating image blurring effects, are (i) the oblique incidence of X-rays since they are emitted by a point source, and (ii) their absorption at various depths within the screen, resulting in slight variations in the fluorescence intensity [6,14,17,19,24,25,32,36–39]. Figure 1 shows SEM images of various granular phosphors.
- (b) Structured (needle-like as shown in Figure 2) crystals that are used as large-area thin screens in various digital imaging detectors (i.e., digital radiography, mammography, portal imaging active-matrix flat panels, etc.). Needle-like crystals (cracks) significantly improve spatial resolution due to limited lateral propagation and the spread of light within the material's mass. Thick screens for improving radiation absorption can be prepared from such materials without degrading spatial resolution. A very popular scintillator in this form that has been used for a long time in image intensifiers (I.Is.) of conventional fluoroscopy systems is CsI:Na (referred to as phosphor in some literature). Another similar material is CsI:Tl. Both CsI:Na and CsI:Tl have been largely used under this form of crystal. The thickness of such screens ranges from 140 μm for digital mammography to 3000 μm for nuclear medicine. The optical sensor part of X-ray digital radiography and mammography detectors, based on CsI, is identical to that used with granular screens (i.e., AMFPI, CCD, CMOS) [17,19,25,37–45].
- (c) Single crystals, usually of large-area transparent layers, are traditionally employed in nuclear medicine (photon counting functional imaging). This form of luminescent material is traditionally referred to as a *scintillator*. In this case, the light spread is not a problem since position accuracy is assured by position-sensitive optical sensor arrays (e.g., PMTs, etc.). NaI:Tl is the most popular in gamma camera and SPECT systems, with a thickness ranging from 6.7 to 12.4 mm. CsI:Tl single crystals are also incorporated in some camera systems. For PET arrays, small single crystals are mostly used, arranged in ring-shaped detectors, with crystal thickness ranging from 10 to 30 mm. The number of crystals may be on the order of tens to hundreds of thousands in total body scanners, with a cross-section of $2 \times 2 \text{ mm}^2$ to $4 \times 4 \text{ mm}^2$ coupled to PSPMT,

- APDs, or SiPM optical sensors. In the case of X-ray CT detectors, where single crystals are often used and arranged in a 2D array in an arc-shaped configuration, the thickness ranges from 0.3 to 3 mm, and the cross-section is on the order of 1 mm. In PET systems, BGO, LSO:Ce, LYSO:Ce, and LGSO:Ce single crystals are considered the most appropriate, principally due to their fast response and high effective atomic number. For CT, CdWO_4 as well as $\text{Gd}_2\text{O}_2\text{S}$ with various activators, i.e., Pr, Ce, and mixtures such as $(\text{Y, Gd})_2\text{O}_3:\text{Eu}$ are mostly preferred. However, a large variety of crystalline materials are currently under investigation [6,18,20,21,26,27,31,34,46–57].
- (d) Transparent ceramics of various scintillators are now produced and incorporated into CT detectors. This form of material in polycrystalline form is produced by various techniques (e.g., sintering of grains of nano-sized powders, generally followed by hot pressure), is of lower cost, and sometimes shows superior light yield and overall better performance than traditional single crystals [31,51,58].
- (e) Storage phosphors (photostimulable materials) are employed in the form of X-ray imaging plates for use in computed radiography. After irradiation, a fraction of the electron/hole pairs do not recombine to transfer their energy to a luminescent center, as in traditional phosphors. In these phosphors, electrons are trapped in metastable states. Only if red wavelength photons interact with these states do the electrons escape to produce luminescence effects. Storage phosphor plates contain grains similar to those used in conventional film–screen radiography and digital radiography. These plates are enclosed in a light-tight cassette, and after being exposed to X-rays, they are read in raster scanning by a laser beam to emit light photons. Computed radiography systems are very successful applications; they can be used with conventional radiography systems and are widely used in hospital radiology departments. The commercially used materials are $\text{BaFBr}:\text{Eu}^{2+}$ and $\text{CsBr}:\text{Eu}^{2+}$ [7,59–62].

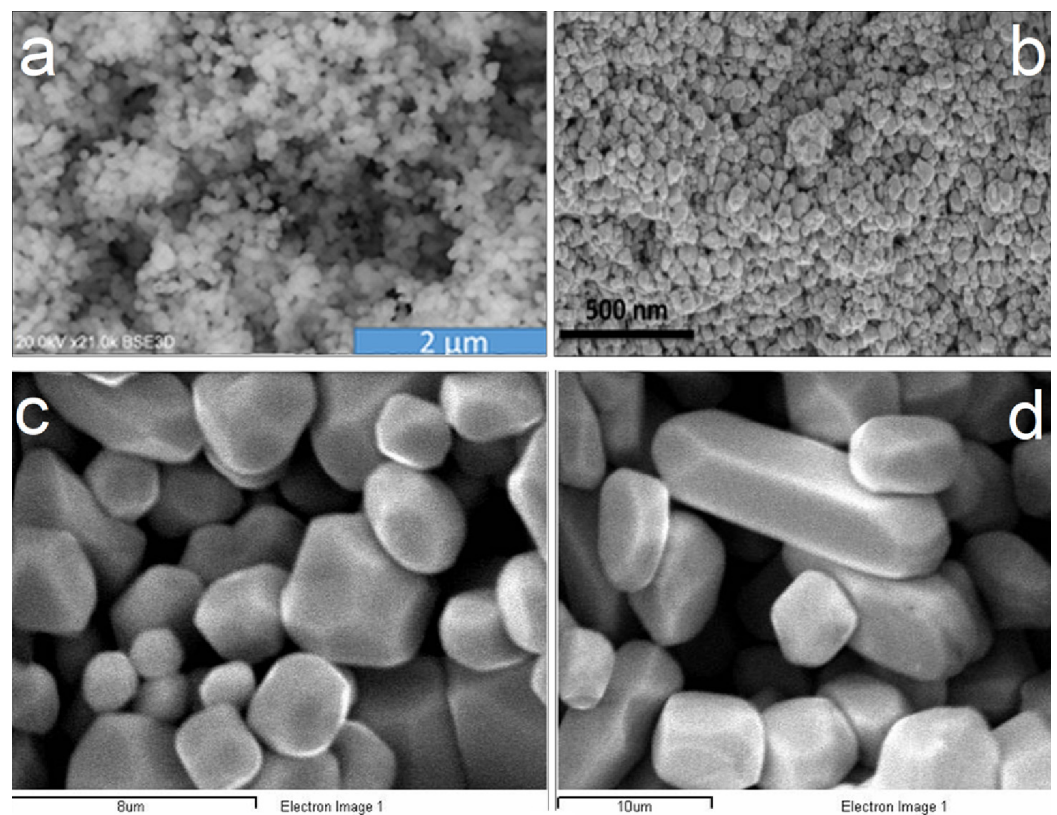


Figure 1. SEM images of various granular phosphors: (a) $\text{Lu}_2\text{O}_3:\text{Eu}$ (mean grain size: 50 nm), (b) $\text{LuPO}_4:\text{Eu}$ (mean grain size: 50 nm), (c) $\text{Gd}_2\text{O}_2\text{S}:\text{Eu}$ (mean grain size: 8 μm), and (d) $\text{Gd}_2\text{O}_2\text{S}:\text{Pr}$ (mean grain size: 8 μm).

- (f) Organic scintillators have been investigated for imaging applications mainly due to their flexibility. Although their absorption efficiency (see below) is generally low, due to their low effective atomic number, light yield on the order of 80,000 photons per MeV has recently been reported for organic powders tested within X-ray imaging settings [63–66].

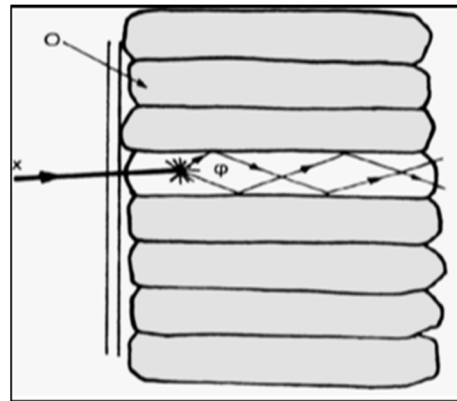


Figure 2. Schematic representation of a structured scintillator showing the propagation of light along a crystal needle (column). The symbol ϕ denotes light photons, and o denotes a needle. x denotes X-ray.

The principal properties considered for evaluating scintillators for medical imaging include the following [4,14,31,32]:

- (i) Radiation absorption and detection efficiency (depending on the effective atomic number, atomic K-shell absorption edge, density of materials, thickness of the particular sample, and energy of incident photons). An index indicating this efficiency is the product ρZ_{eff}^4 (ρ : density, Z_{eff}^4 : effective atomic number). Absorption and detection efficiency are very crucial for capturing a significant fraction of the incident radiation (input signal) as well as for reducing the radiation dose burden to the patient (less radiation for a given level of output signal).
- (ii) The intrinsic conversion efficiency of radiation energy into light within the material's mass or light yield (depending on the forbidden energy gap and other intrinsic material parameters) [35,67,68]. This parameter expresses the capability of a material to use efficiently the absorbed radiation energy.
- (iii) Light transmission efficiency and the distribution of light at the material's emitting surface (depending on the transparency, index of refraction, and light scattering properties of the material as well as on the thickness of the particular scintillator sample). In the case of granular phosphor screens, light scattering can be useful since it may reduce the extent of light spreading that deteriorates the point-by-point projection in X-ray radiographic and fluoroscopic imaging. On the other hand, in large-area transparent single crystals, usually employed in nuclear medicine, light is distributed in the whole scintillator mass. However, this is not a serious problem, due to the one-by-one photon counting and the use of position-sensitive optical sensors. In these techniques, high transparency is important since it improves light collection by the optical sensors. In some cases (e.g., in X-ray radiography), the thickness of the scintillating layer may decrease the transparency as well as the light transmission and emission, similarly affecting the quality of the final image. Additionally, thick scintillating layers (screens) contribute to a widening of the spread of the light photons that manage to reach their surface, thus reducing spatial resolution. This is shown in Figure 3, which depicts the distribution of light photons at the rear (emitting) surface of two granular phosphor layers of different thicknesses of 100 and 300 μm , respectively. These data were obtained by Monte Carlo methods (see Section 3.1.), assuming a pencil-like monoenergetic ionizing radiation beam absorbed at a single

point within the scintillator layer. This distribution of light photons defines the so-called point spread function (PSF), which is an expression of the spatial resolution of an imaging system.

- (iv) The spectrum of emitted light (determined by the energy levels of the activator). This spectrum should match, as closely as possible, the quantum spectral sensitivity distribution of the optical sensor.
- (v) The emission of K-characteristic X-ray fluorescence after photoelectric absorption. This kind of emission may be a disadvantage in planar projection imaging if its absorption occurs within the phosphor–scintillator mass at a point different from that of X-ray or gamma-ray initial incidence.
- (vi) Decay time (determined by the probability of electric dipole transitions and being proportional to the light photon wavelength) [67]. Detectors employed in X-ray fluoroscopy, CT, and in nuclear medicine (particularly in PET) should be as fast as possible, thus requiring short or very short decay time. This can be accomplished by phosphors–scintillators emitting in the blue or ultraviolet spectral region.
- (vii) Energy resolution (X- and gamma-ray spectral resolution depending on light yield and non-proportionality effects in the response of some materials below 100 keV) [31].
- (viii) Afterglow (i.e., non-principal emission components with a relatively long decay time).
- (ix) Hygroscopicity.
- (x) Fragility.

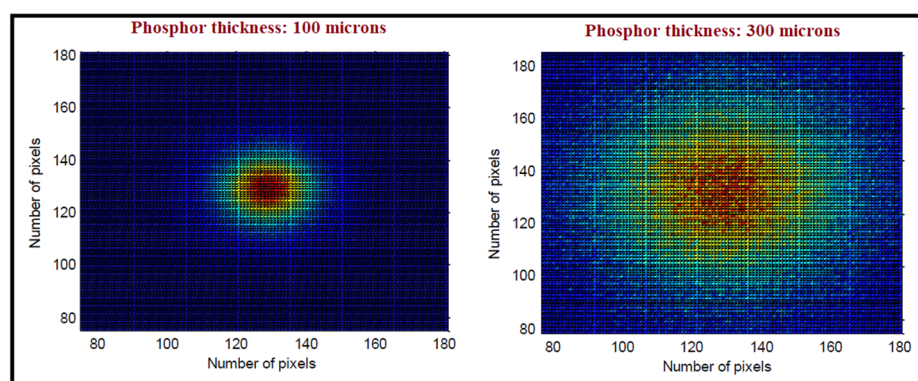


Figure 3. Spatial distribution (spread) of light photons at the surface of two phosphor layers of different thicknesses.

Absorption efficiency, intrinsic conversion efficiency, and light transmission efficiency are principal factors determining the overall luminescence efficiency of a luminescent material. This efficiency is of primary importance for both image quality and patient dose burden in clinical conditions. Table 1 shows properties of some well-known luminescent materials.

Table 1. Properties of some popular scintillators and phosphors, ρ : density, LY: light yield. Data were obtained from [13,15].

Scintillator/Phosphor	ρ (g/cm ³)	ρZ_{eff}^4	LY (Light Photons per MeV)	Wavelength (nm)	Decay (ns)	Hygro	Afterglow
CaWO ₄	6.1	89	20,000	420		No	No
Gd ₂ O ₂ S:Tb	7.3	103	60,000	545	10 ⁶	No	No
CsI:Na	4.5	38	40,000	420	630	Yes	No
CsI:Tl	4.51	38	54,000–66,000	550	1000	Yes	Yes
CdWO ₄	7.9	134	28,000	495	2.15 × 10 ³	No	Slight
Gd ₂ O ₂ S:Pr, Ce, F	7.3	103	35,000	510	4 × 10 ³	No	Slight
Gd ₂ O ₂ S:Pr (UFC)	7.3	103	50,000	510	3 × 10 ³	No	Slight
NaI:Tl	3.67	24.5	38,000	415	230	Yes	No

Table 1. Cont.

Scintillator/Phosphor	ρ (g/cm ³)	ρZ_{eff}^A	LY (Light Photons per MeV)	Wavelength (nm)	Decay (ns)	Hygro	Afterglow
Bi ₄ Ge ₃ O ₁₂ (BGO)	7.1	227	9000	480	300	No	No
Lu ₂ SiO ₅ :Ce(LSO)	7.4	143	26,000	420	40	No	No
Gd ₂ SiO ₅ :Ce(GSO)	6.7	84	8000	440	60	No	No
YAlO ₃ :Ce(YAP)	5.5	7	21,000	350	30	No	No
LaCl ₃ :Ce	3.86	23.2	46,000–50,000	330	24 (60%)	Yes	No
LaBr ₃ :Ce	5.03	25.6	61,000–70,000	358	16	Yes	No

2.1. Detector Signal

The signal produced by an imaging system can be expressed as a product of various signal-converting stages, g_i , in the following form [6,24,69–71]:

$$S_{out}(E, x, y) = \Phi_{\Lambda} = \prod_i g_i(E, x, y) \Phi \quad (1)$$

where Φ denotes the number of photons per unit of area of incident radiation photons and Φ_{Λ} is the fluence of output light photons (or other information carriers) produced at the detector output. E, x, y denote the energy of X-ray or gamma-ray photon and spatial coordinates, respectively. In the case of X-ray imaging, where an energy spectrum is used and the signal is proportional to this energy, the following form is more appropriate:

$$S_{out}(x, y) = \int_0^{kV} \frac{d\Psi(E)}{dE} \prod_i g_i(E, x, y) dE \quad (2)$$

where Ψ is the energy fluence of the incoming radiation, E is the X-ray photon energy, and $d\Psi(E)/dE$ is the spectral density of the radiation spectrum. g_i are gain factors expressing the conversion of the input signal at the various stages of signal transmission through the detector system [72–77]. In the case of Equation (1), the gain factors express the number of information carriers (photons or charges) or fractions of such numbers, while in Equation (2), the gain factors express energy or fractions of energy, e.g., g_1 represents the detection of X-rays given by the quantum detection efficiency (QDE) or by the energy absorption efficiency (EAE) [22]. QDE is the fraction of incoming photons missing from the photon beam exiting the scintillator's rear surface, while EAE corresponds to energy losses within scintillator's mass. QDE is given as:

$$g_1(E) = \eta_Q = QDE(E) = (1 - e^{-(\mu_{tot,t}(E)/\rho)w}) \quad (3)$$

where $\mu_{tot,t}(E)$ is the total mass X-ray attenuation coefficient of the scintillator material. EAE is calculated as:

$$g_1(E) = \eta_E = EAE(E) = \left(\frac{\mu_{tot,en}(E)}{\mu_{tot,t}(E)} \right) (1 - e^{-(\mu_{tot,t}(E)/\rho)w}) \quad (4)$$

where $\mu_{tot,en}(E)$ is the total mass energy absorption coefficient and w is the crystal thickness (surface density). The coefficient of energy absorption corresponds to the average fraction of the kinetic energy of secondary electrons that is locally deposited in the detector mass and takes into account radiative losses due to Bremsstrahlung radiation by electrons as well as K-fluorescence effects [22]. The coefficients of total attenuation and energy-absorption depend on the effective atomic number of the material and can be obtained from databases. In the case of broad-spectrum beams used in diagnostic radiology, QDE and EAE are averaged over the X-ray spectrum (i.e., $d\Phi(E)/dE$ and $d\Psi(E)/dE$, respectively) [78,79]. As it can be seen from the above relations, the thickness w of the scintillation layer is important for the incident radiation absorption.

Figure 4 shows data on the energy absorption efficiency for various scintillator crystals under irradiation by a spectrum of X-rays at tube voltages up to 140 kVp. The values of EAE range from approximately 0.30 to 0.90. These values are clearly higher than the corresponding efficiency of traditional granular Gd_2O_2S radiographic screens, ranging from 0.1 to 0.5–0.6. The shape of the curves is determined by the variation in $\mu_{tot,en}(E)/\rho$, which, however, is not clearly shown due to the presence of a spectrum of energies (instead of monoenergetic photons), i.e., the values of EAE are averaged over this spectrum. BGO shows very high values due to its high effective atomic number and density.

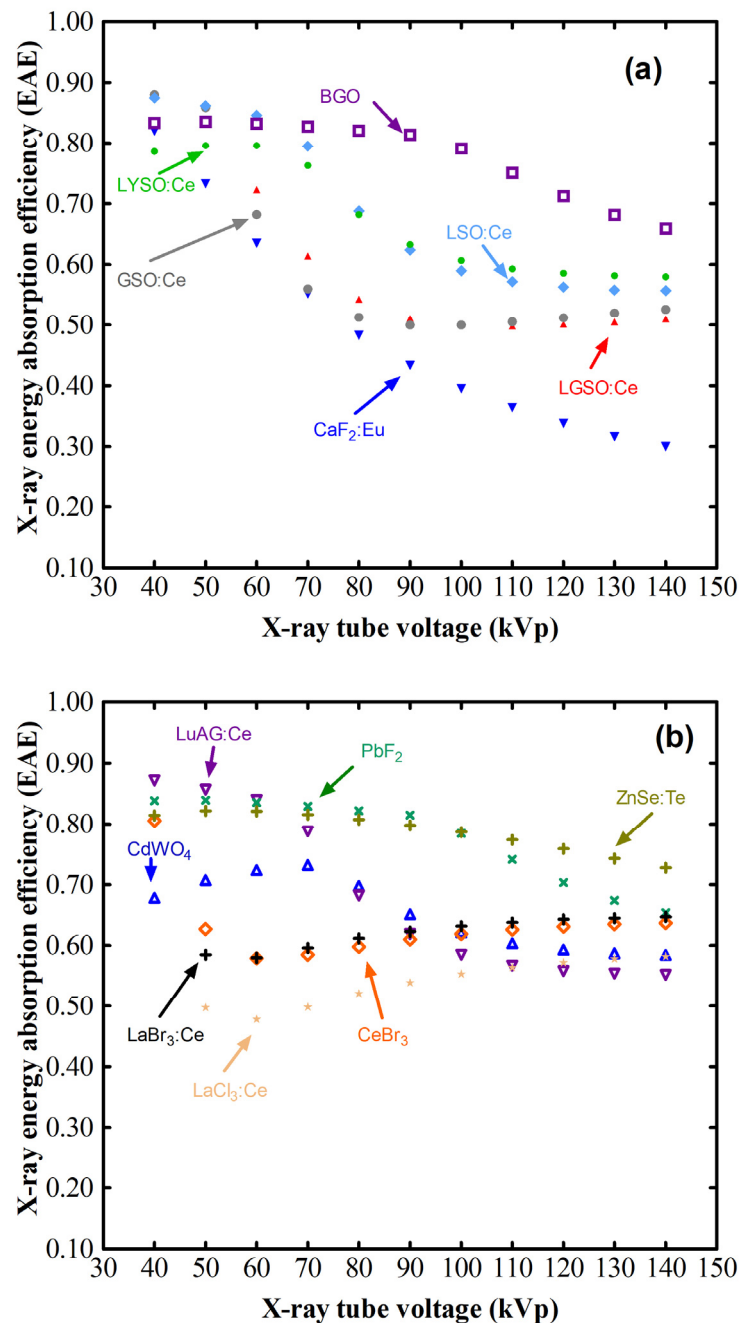


Figure 4. (a,b) Energy absorption efficiency for various scintillator materials. Data are calculated according to [22] considering polyenergetic X-rays. The BGO crystal shows highest absorption efficiency due to its very high effective atomic number and density (ρZ_{eff}^4).

The gain factor g_2 represents the intrinsic conversion efficiency (ICE) of the material [70]. This efficiency (η_c) is approximated as:

$$g_2 = \eta_c = \frac{h\bar{\nu}}{\beta E_g} S Q \quad (5)$$

where $h\bar{\nu}$ is the mean energy of light photons and βE_g is the energy that must be transferred by a photoelectron to create an electron–hole pair in the scintillator material. E_g is the energy band-gap between the valence and the conduction energy bands [4,18,67,68]. β is a parameter related to energy losses due to lattice vibrations. S is a transfer efficiency of energy to the luminescent center, and Q is the quantum efficiency of the luminescent center. The values of ICE range from 0.03 to more than 0.20 depending on the forbidden energy gap of the material [70].

The gain factor g_3 is the light transmission efficiency (LTE), while g_4 denotes the spread of light photons in the output scintillator surfaces. g_5 is the conversion of light into electrons within the optical sensor, etc.

Finally, the emitted light energy flux Ψ_Λ is taken as the output signal S_{out} . Alternatively, the light photon flux Φ_Λ has also been used in many studies. In these cases, the spectral density corresponds to photons per unit of area [$d\Phi(E)/dE$] and the gain g_2 is the light yield, i.e., the number of light photons created within the scintillator mass per absorbed X-ray, $g_2 = m_\lambda = \eta_c \bar{E}/h\bar{\nu}$. In contrast to η_c , which has values much lower than 0.5, the light yield m_λ is expressed in numbers of photons that are on the order of a few thousand.

In the case of photon-counting detectors, a series of output pulses is produced, each one representing an X- or gamma-ray photon absorbed in the detector. The amplitude V of each pulse is directly proportional to the energy E of the corresponding photon absorbed in the detector.

$$V(E) = \left(\frac{E}{h\nu}\right) \prod_i g_i \quad (6)$$

where $h\nu$ is the energy of the light photons created in the scintillator and g_i are the gain factors of the signal conversion stages.

A stage in optical signal transmission is the detection of the light photons by the optical sensor. The spectral sensitivity of the optical sensor and the emission spectrum should be suitably matched. This matching can be estimated by the spectral matching factor expressing the capability of an optical sensor to detect the emitted light photons of a phosphor. This factor is defined as:

$$a_s = \int_{\Delta\lambda} \varphi_p(\lambda) S_d(\lambda) d\lambda / \int \varphi_p(\lambda) d\lambda \quad (7)$$

where $\varphi_p(\lambda)$ is the emitted light spectrum of the scintillator–phosphor, $S_d(\lambda)$ is the spectral distribution of quantum efficiency or spectral sensitivity of the optical detector coupled to the phosphor, and $\Delta\lambda$ is the spectral range of the emitted light. Figure 5 shows light spectra of various materials and the quantum efficiency (spectral sensitivity) curves of some optical sensors. Table 2 is a list of spectral matching factor values.

Table 2. Values of the spectral matching factor for various luminescent materials and optical sensor combinations.

Optical Detectors	CaF ₂ :Eu	CdWO ₄	CeBr ₃	ZnSe(Te)	LGSO:Ce	LuAG:Ce	LaBr ₃ :Ce	LaCl ₃ :Ce
CCD broadband AR coating	0.94	0.97	0.76	0.91	0.94	0.97	0.65	0.22
CCD infrared (IR) anti-reflection (AR) coating	0.54	0.69	0.42	0.92	0.57	0.77	0.37	0.14
CMOS hybrid with blue anti-reflection (AR) coating	0.60	0.74	0.51	0.94	0.63	0.81	0.31	0.05
Hybrid CMOS blue	0.79	0.93	0.63	0.99	0.82	0.98	0.38	0.06
CMOS (monolithic 0.25 μm)	0.64	0.84	0.32	0.96	0.67	0.92	0.20	0.02
a-Si:H passivated	0.63	0.75	0.55	0.77	0.66	0.80	0.24	0.02
a-Si:H_non-passivated	0.92	0.97	0.84	0.85	0.93	0.99	0.38	0.03

Table 2. Cont.

Optical Detectors	CaF ₂ :Eu	CdWO ₄	CeBr ₃	ZnSe(Te)	LGSO:Ce	LuAG:Ce	LaBr ₃ :Ce	LaCl ₃ :Ce
CCD with indium tin oxide (ITO) gates with microlenses	0.68	0.78	0.58	0.96	0.70	0.83	0.44	0.12
CCD with indium tin oxide (ITO) gates	0.51	0.68	0.39	0.90	0.55	0.75	0.30	0.08
CCD with polygates	0.18	0.46	0.03	0.78	0.24	0.59	0.02	0.00
CCD no poly-gate LoD	0.34	0.66	0.19	0.87	0.43	0.82	0.03	0.00
CCD with traditional poly gates	0.34	0.70	0.20	0.88	0.46	0.87	0.03	0.00
CMOS (photogate array 0.5 μm)	0.26	0.60	0.14	0.91	0.37	0.76	0.20	0.02
CMOS RadEye HR	0.68	0.82	0.05	0.97	0.75	0.89	0.00	0.00
GaAs photocathode	0.95	0.96	0.94	0.99	0.95	0.97	0.94	0.93
GaAsP phosphor photocathode	0.52	0.76	0.35	0.79	0.58	0.84	0.34	0.27
Extended photocathode (E-S20)	0.94	0.85	0.95	0.60	0.94	0.78	0.94	0.83
Si PM MicroFC-30035-SMT	0.94	0.72	0.86	0.34	0.88	0.59	0.85	0.66
Si PM MicroFB-30035-SMT	0.92	0.66	0.78	0.30	0.85	0.52	0.76	0.55
Si PM MicroFM-10035	0.61	0.88	0.34	0.67	0.70	0.89	0.09	0.00
Si PM S10985-050C	0.95	0.87	0.86	0.55	0.95	0.79	0.85	0.67
Si PM S10362-11-025U	0.96	0.85	0.86	0.54	0.94	0.77	0.85	0.67
Si PM S10362-11-050U	0.95	0.87	0.82	0.55	0.95	0.79	0.81	0.62
Si PM S10362-11-100U	0.96	0.86	0.88	0.52	0.95	0.78	0.86	0.65
Flat panel PS-PMT H8500C-03	0.91	0.56	0.99	0.08	0.82	0.38	0.98	0.93
Flat panel PS-PMT H8500D-03	0.78	0.43	0.95	0.05	0.69	0.30	0.95	0.99
Flat panel PS-PMT H10966A	0.79	0.43	0.96	0.05	0.70	0.29	0.96	0.99
Flat panel PS-PMT H8500C	0.86	0.53	0.97	0.07	0.79	0.37	0.96	0.91
Bialkali photocathode	0.78	0.45	0.95	0.06	0.70	0.31	0.95	0.94
Multialkali photocathode	0.81	0.64	0.97	0.36	0.79	0.58	0.97	0.99

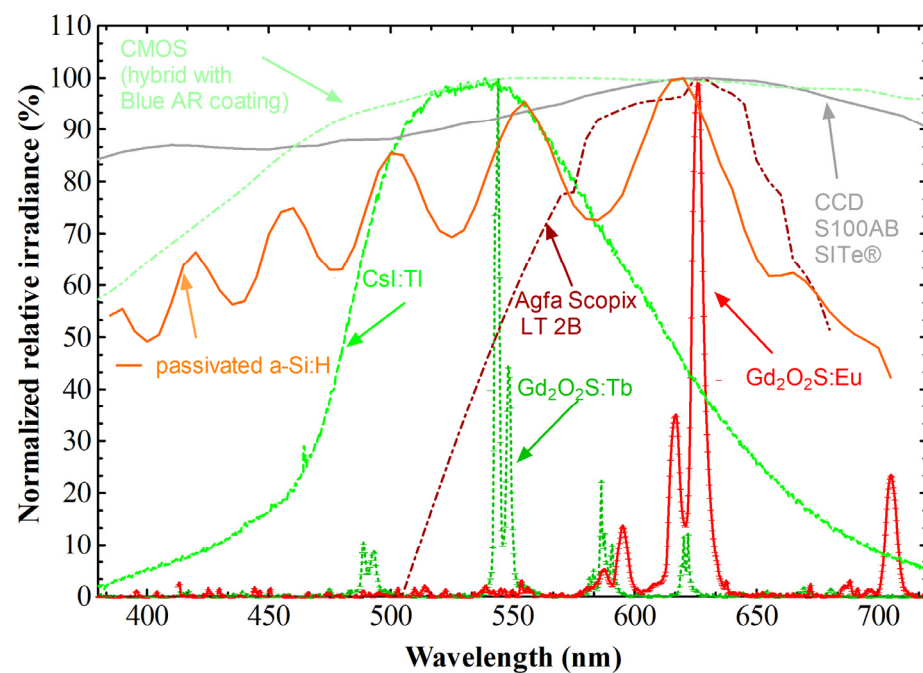


Figure 5. Light emission spectra and spectral sensitivity curves of various luminescent materials and optical sensors.

2.2. Noise and the Signal-to-Noise Ratio

Medical imaging systems detect a signal in a noisy background and are referred to as *quantum limited systems*, where noise plays an important role in the formation of the final image [80]. Noise has been expressed as the sum of variances in the processes in various stages of signal transmission. To analyze such processes, Poisson statistics have

been assumed for X-ray and light photons and the binomial probability distribution has been assumed for X-ray detection and light transmission [69,72]. E.g., the variance in a binomial distribution may be written as:

$$\sigma_{g_i}^2 = g_i(1 - g_i) \quad (8)$$

where g_i is taken as the mean value of either quantum detection efficiency or /and light transmission efficiency. Under this assumption, the effect of noise is expressed as the variance in the number of light photons, given as:

$$\sigma_{\lambda}^2 = \bar{\Phi}g_1(g_2g_3)^2 + \bar{\Phi}g_1g_2g_3 \quad (9)$$

Since medical imaging systems detect signals in a noisy background, it is of primary importance to determine the signal-to-noise ratio (SNR). The latter is often expressed as the detective quantum efficiency (DQE), defined by the ratio $(SNR_{output}/SNR_{input})^2$, but has also been expressed by the relation [17,19,24]:

$$DQE(E) = \eta_Q A_S = g_1 \frac{m_1^2}{m_0 m_2} \quad (10)$$

where A_S is a parameter expressing the statistical fluctuations in the number of emitted light photons per absorbed incident photon, often called the statistical factor or the Swank factor. m_i are the moments of the statistical distribution of the number of light photons emitted per X-ray absorbed. For a perfect detector, $A_S = 1$. The DQE, defined in this way, is referred to as zero-frequency DQE and takes into account the fluctuation in the detector signal per incident photon. Such fluctuations appear, although these incident photons may be of equal detected energy. The K-fluorescence effect (i.e., emission of characteristic X-rays after photoelectric absorption) and Lubbert's effect (i.e., absorption of photons at different depths create variations in signal spreading) are among the various noise sources affecting output noise [81]. In the case of polyenergetic X-ray beams, the corresponding spectrum must be taken into account.

3. Methodology of Research

3.1. Theories

Imaging detectors are analyzed within the framework of signal and noise transmission analysis in both space and spatial frequency domains [64,70–76]. Various quality metrics, such as the emission efficiency, the MTF, the NPS, and the DQE have been evaluated by theoretical models and experimental techniques. The prevailing theory in the analysis of these parameters is traditionally based on *linear cascaded systems analysis* (LCS) [73–76]. In this analysis, a radiation detector is assumed to be approximately, linear or linearizable, stationary, and ergodic. In stationary systems, the functions describing the signal or noise transfer are independent of the specific point on the detector surface at which they are measured. In ergodic systems, the average value of measurements at various points in the image is equal to the average value of repeated measurements at the same point.

A full imaging system is assumed to consist of a number of *cascaded stages*, each one corresponding to a particular physical process contributing to the creation of an image (see Equations (1) and (2)). The *output* (both signal and noise) of a particular stage is fed to the input of a subsequent stage. The *input signal* to the system is the incident X-ray fluence, and the *output signal* of the complete system is the emitted light fluence (*luminescence*). The *input noise* is the variance in the spatial distribution of the incident photons, and the *output noise* is the variance in the spatial distribution of the emitted photons. The various intermediate stages are divided into: (i) *quantum gain stages*, corresponding to the conversion or amplification of signal carriers and (ii) *spreading or blurring stages*, describing the spreading of carriers. According to statistics and signal spatial dislocation, blur stages can be also categorized as either *stochastic* or *deterministic*. Gain stages are characterized by an *average gain* (\bar{g}_i) and an *average gain variance* ($\sigma_{g_i}^2$). Blurring stages are characterized by

an MTF, which expresses the degree of spreading and affects the spatial resolution in the final image.

An MTF also appears in the noise power spectrum expression, as previously analysed by [69]:

$$NPS(u, v) = \bar{\Phi}_\Lambda \left[(g_2 g_3) MTF^2(u, v) + 1 \right] \tag{11}$$

where $\bar{\Phi}_\Lambda$ is light photon fluence and u, v are spatial frequencies. The first term of the above equation is expressed as the *correlated noise component*, while the second term (i.e., $\bar{\Phi}_\Lambda$) is referred to as the *uncorrelated noise component* [69,71]. In the case of X-ray beams exhibiting a broad spectrum (as in diagnostic radiology), the NPS should be averaged over this spectrum.

The *signal detection theory* (SDT) [77,78,82], assuming that a human observer detects signals in a noisy background, is also employed in imaging detector analysis. In this theory, the *threshold contrast* C_T (i.e., the minimum contrast detectable by a human observer) and the objective SNR, which depends on scintillator properties, are entangled in the following formulation:

$$C_T \geq k \frac{\sigma}{\bar{\Phi}} = k C_N = \frac{k}{\sqrt{\bar{\Phi}}} = \frac{k}{SNR} \tag{12}$$

where k is the observer’s threshold signal-to-noise ratio, which depends on the detection probability assumed by the observer (Rose model).

The physical processes in luminescent materials related to imaging have been described by theoretical models, either based on the differential diffusion equation, on geometrical optics, or on Monte Carlo techniques [76,78,82,83]. Within the framework of the diffusion equation, the light transmission efficiency g_3 and g_4 in Equations (1) and (2) are given as:

$$g_3(E)g_4(E) = \int_0^{w_0} \bar{\phi}_X(E, w) \bar{g}_\lambda(\sigma, \tau, \rho, w) dw dE \tag{13}$$

where w_0 is the scintillator thickness (in the form of a screen). In this formulation, it is assumed that the scintillator consists of a large number of superimposed elementary thin layers of thickness dw . w is the depth of each thin layer. The function $\bar{\phi}_X(E, w)$ expresses the relative probability of X-ray absorption at a depth w . The function $\bar{g}_\lambda(\sigma, \tau, \rho)$ is a solution of the photon diffusion differential equation (in the framework of Swank theory) [70,76]:

$$\bar{g}_\lambda(\sigma, \tau, \rho) = \frac{\tau \rho_1 [(\sigma + \tau \rho_0) e^{\sigma w} + (\sigma - \tau \rho_0) e^{-\sigma w}]}{(\sigma + \tau \rho_0)(\sigma + \tau \rho_1) e^{\sigma w_0} - (\sigma - \tau \rho_0)(\sigma - \tau \rho_1) e^{-\sigma w_0}} \tag{14}$$

where σ and τ are the reciprocal of the light photon diffusion length and the inverse relaxation length, which are functions of the optical scattering and the optical absorption coefficients. In the spatial frequency domain, σ is given as $\sigma = \sigma_0^2 + 4\pi v^2$, where σ_0 corresponds to zero frequency and ρ_0, ρ_1 are reflectivity parameters corresponding to the reflection of light at the front and back scintillator surfaces, respectively. As it can be seen that light propagation is affected exponentially by the total phosphor–scintillator thickness w_0 . According to LCS analysis, g_3 corresponds to the deterministic gain stage expressing the fraction of X-rays converted into emitted light, while g_4 expresses a spreading and stochastic stage of signal conversion (i.e., due to isotropic light generation and scattering).

For single crystals, and assuming that equal numbers of optical photons travel in both the forward and backward directions within the crystal’s mass, a corresponding function has been found [36,37]:

$$\bar{g}_\lambda(R, k) = (1 - R_0) \left[\frac{k^{N-n}}{1 - k^{2N} R_0 R_1} + R_1 k^{n+N} + \frac{k^{2N} R_0 R_1}{1 - k^{2N} R_0 R_1} \right] \tag{15}$$

where R_0 is the output reflectivity, R_1 is the input reflectivity, and k is the light attenuation coefficient [84].

In addition to analytical modeling, Monte Carlo methods, based on Mie light scattering effects within scattering media [85] for evaluating granular phosphors, GATE software Version 5.0 for crystals [86] or GEANT for granular screens [87], have been used [74,88,89].

In Mie scattering theory, the so-called light extinction efficiency factor Q_{ext} , which plays an important role in the physical processes, is defined as follows:

$$Q_{ext} = \frac{2}{x^2} \sum_{n=1}^{\infty} (2n+1) \operatorname{Re}(a_n + b_n) \quad (16)$$

where x is the size parameter of Mie theory, which is a function of the complex refractive index of the phosphor material and of the light wavelength. a_n and b_n are the Mie coefficients, which are functions of the complex refractive index of the medium surrounding the phosphor grains. Details can be found in [90].

3.2. Definitions of Quality Metrics

The imaging performance of phosphors–scintillators and the corresponding imaging detectors is evaluated by various physical quantities quantifying the emission intensity, the spatial resolution, and the noise as well as the signal-to-noise ratio [70,76,77,91–98].

3.2.1. Luminescence Emission Efficiency

The emission efficiency of a scintillator is expressed by the luminescence efficiency (LE), which is defined as the emitted light energy fluence per unit of incident radiation energy fluence:

$$\eta_{\Psi} = \Psi_{\Lambda}(\Delta\lambda) / \Psi_0(E_0) \quad (17)$$

and corresponds to the multiplication of the three stages $g_1(E)g_2g_3(E)$ (in Equation (2)). In the case of X-rays, this is integrated over the X-ray spectrum, $\Delta\lambda$ is the light spectrum range of the emitted light, and E_0 is the X-ray tube voltage. The X-ray luminescence efficiency is often expressed with the experimentally determined absolute efficiency (AE), η_A , defined as the ratio of emitted light energy fluence, Ψ_{Λ} , over the incident exposure X ,

$$\eta_A = \Psi_{\Lambda}(\Delta\lambda) / X(E_0) \quad (18)$$

AE is expressed in efficiency units (EU, 1 EU = $\mu\text{Wm}^{-1} / \text{mR}$) (Figure 6).

Figures 6 and 7 show experimental data (see Section 3.3) on the absolute efficiency and X-ray luminescence efficiency, respectively, of various crystals. As it can be observed, the fraction of incident energy converted into light energy is very low, ranging from approximately 0.001 to 0.013. The shape of the curves as well as the LE values are affected by a combination of the effects of EAE, ICE, and LTE, and all these efficiencies are clearly lower than unity. This shape shows only slow variations due to two opposing trends: (a) EAE tends to decrease with the increasing energy (kVp) of incident photons since they become more penetrating and either penetrate the crystal or are absorbed at great depth from the surface. (b) Therefore, the photons of light created at this depth will have to travel short distances before their emission, thus increasing LTE. In any case, these results show that scintillators are not very efficient energy converters.

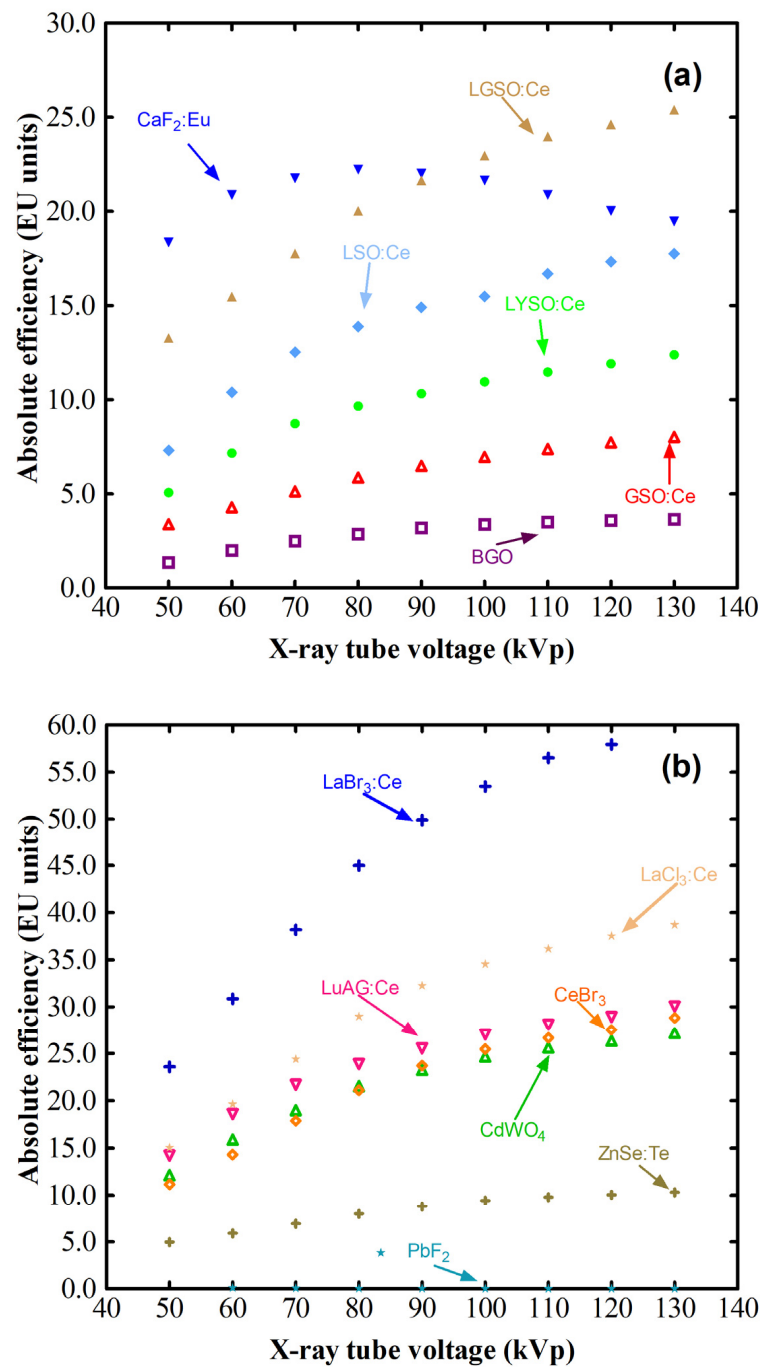


Figure 6. (a,b) Absolute luminescence efficiency data for various single crystal scintillators in the X-ray diagnostic energy range. The measurements were performed according to the methods described in the text. The shape of the curves is determined by the corresponding variations in absorption efficiency and light transparency.

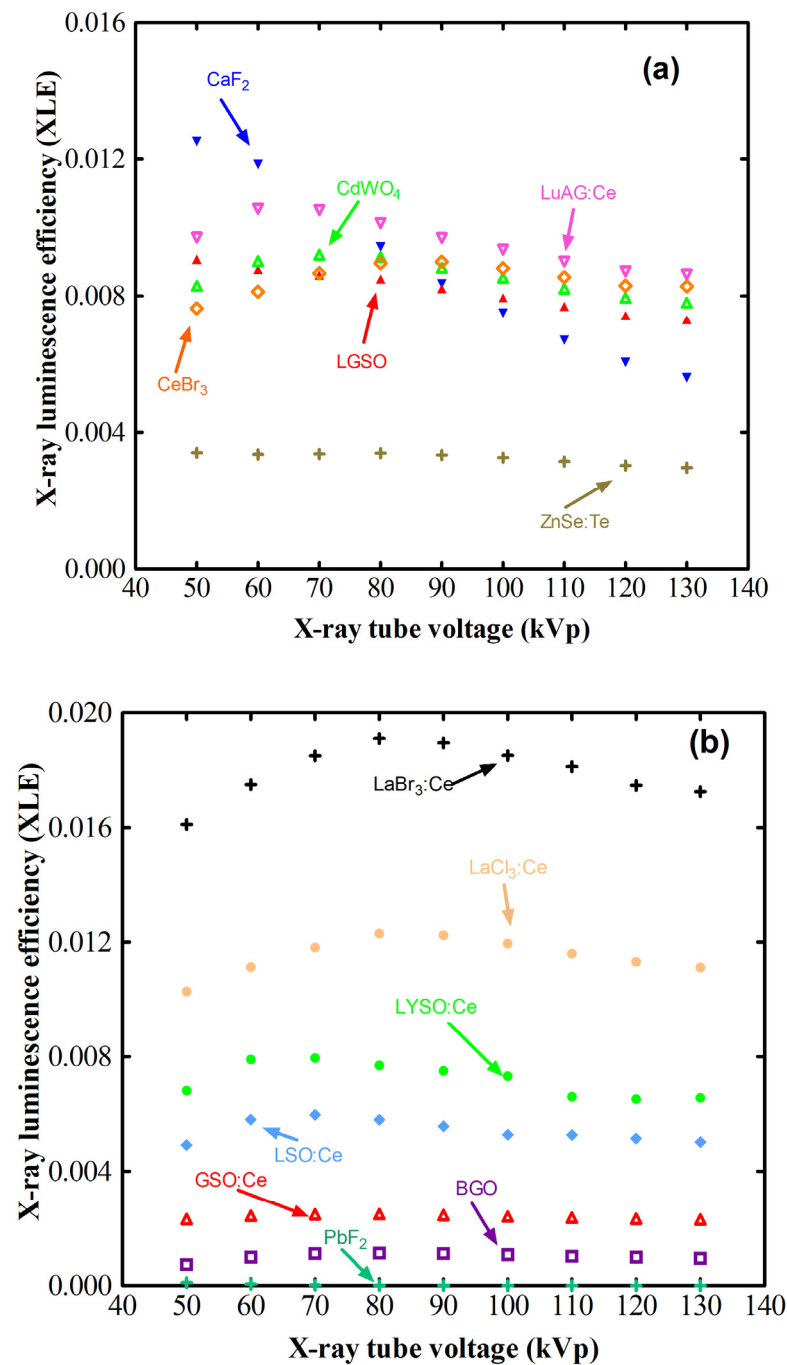


Figure 7. (a,b) Data on the luminescence efficiency of various materials in the diagnostic energy range. The LE values express the fraction of incident radiation energy converted into emitted light. The exposure data were converted into energy fluence data as described in the text. This conversion affects the shape of the curves, which now reflect more appropriately the energy conversion and energy loss mechanisms within the materials' mass. The curves show a tendency to decrease with increasing X-ray tube voltage. As can be seen, the fraction of incident energy converted into emitted light is very low, i.e., on the order of 0.001 to 0.013 approximately.

3.2.2. Modulation Transfer Efficiency

A scintillator's imaging performance is determined by the signal and noise transfer properties of the material. The efficiency to transfer a signal is usually expressed by the modulation transfer function [41,75–77,91–94,98,99], defined by the output signal (light

photon fluence), expressed in the spatial frequency domain and normalized to zero spatial frequency ($\nu = 0$):

$$MTF(\nu) = \Phi_{\Lambda}(\nu) / \Phi_{\Lambda}(0) \quad (19)$$

Since Φ_{Λ} expresses light photon fluence, the MTF is given as the fraction of the light photons corresponding to spatial frequency ν . In this sense, the output signal may be expressed in the spatial frequency domain in terms of the MTF:

$$\Phi_{\Lambda}(E_0, \nu) = M(E_0, \nu) \left[\int_0^{E_0} [d\Phi(E)/dE] g_1(E) g_2(E) g_3 g_4(E, \sigma, \tau, \nu) dE \right] \quad (20)$$

The above expression corresponds to polyenergetic X-rays and is integrated over the X-ray spectrum and E_0 is the maximum photon energy determined by the X-ray tube voltage. The MTF expresses both image contrast (in the low-to-medium frequency range) and spatial resolution (values in the high spatial frequency range correspond to small dimensions in the space domain).

Figure 8 shows experimental MTF data for various phosphors–scintillators in granular form or structured (cracks) form (CsI:Tl). The thickness of the samples corresponds to those often found in diagnostic radiology departments. $\text{Lu}_2\text{O}_3\text{:Eu}$ and CsI:Tl show high MTF values, particularly in the high spatial frequency region, corresponding to improved spatial resolution. It should be emphasized, however, that although CsI:Tl is very thick, it retains good spatial resolution performance due to its structured form. $\text{Gd}_2\text{O}_2\text{S:Tb}$ also shows high MTF values, particularly in the high-frequency range.

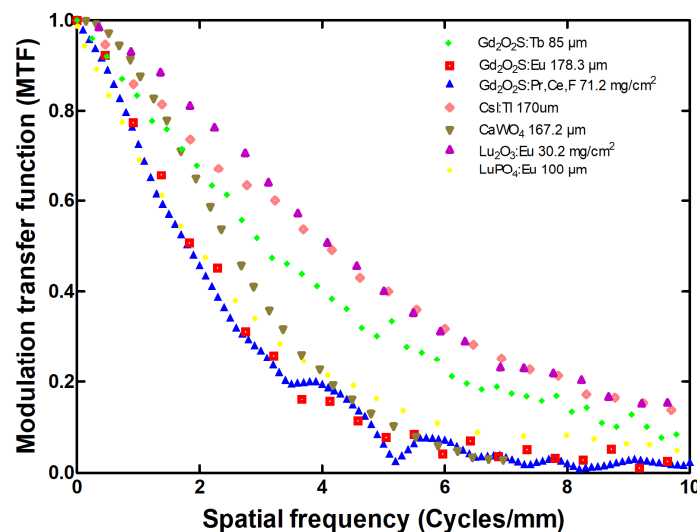


Figure 8. MTF curves for various phosphors–scintillators in granular form or structured (cracks) form (CsI:Tl). The thickness of the samples corresponds to those usually employed in diagnostic radiology departments.

3.2.3. Noise and Signal-to-Noise in the Spatial Frequency Domain

Noise can be expressed in the spatial frequency domain by the noise power spectrum [75,77,91–94,98,99]. The NPS is determined by Fourier transforming the signal differences obtained under the uniform irradiation of the scintillator. Analytically, the NPS has also been expressed in terms of g_1, g_2 , and $g_3 g_4$ (see Equation (11)).

The overall performance of the imaging process is expressed via spatial frequency-dependent detective quantum efficiency [38,69,71,75,77,91–94], which is defined as the

efficiency in transferring SNR through an imaging system. For a scintillating screen, DQE may be written as:

$$DQE(v) = \frac{(\Phi_{\Delta} MTF(v))^2}{NPS(v) SNR_{in}^2} \quad (21)$$

The variation in DQE with increasing spatial frequency follows the ratio $MTF^2(v)/NPS(v)$, which decreases with frequency since the MTF reduces to low values faster than the NPS [69,71]. The values of DQE at low spatial frequencies may vary from 0.10 to 0.50 for Gd_2O_2S phosphor screens [100]. Such values show that the signal-to-noise ratio decreases but to a lesser extent with respect to energy conversion.

Figure 9 shows data for zero-frequency DQE , QDE , and the Swank factor for a $Gd_2O_2S:Tb$ phosphor screen employed in X-ray conventional and digital mammography. The curves were determined by Equation (10) using Monte Carlo methods [90]. A monoenergetic beam was assumed with energy varying from 20 to 70 keV. As can be seen, the DQE values range from nearly 0.6 to 0.1, while QDE shows a similar behavior but with higher values. The energy of the K-absorption edge of Gd at 50.2 keV is clearly shown. It is worth noting that the efficiency of SNR transfer through the imaging system is clearly higher than the efficiency of energy conversion as expressed by LE. This may be explained by taking into account that LE represents the fraction of energy, while DQE is determined through physical quantities expressed in the number of photons (see Equations (11), (19) and (20), i.e., despite the fact that the energy shows only losses through the stages, the number of photons or other information carriers increase in some stages, e.g., in the second stage of signal conversion, where one incident photon is converted into thousands of light photons.

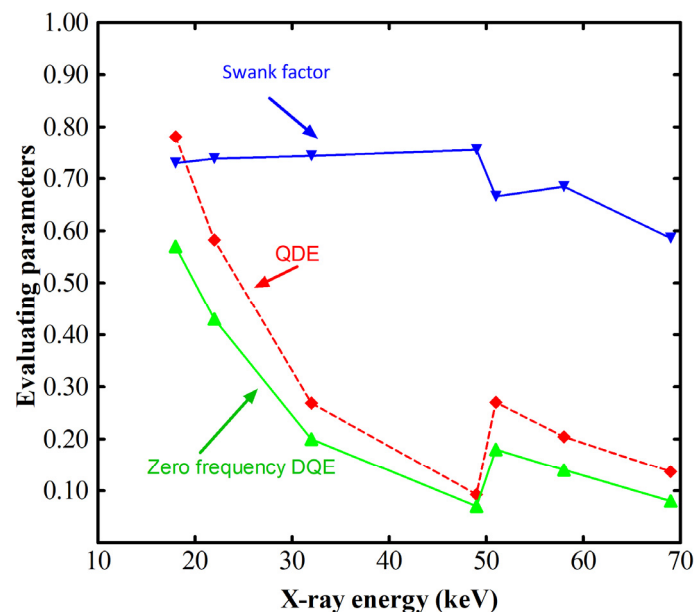


Figure 9. Zero-frequency DQE , QDE , and the Swank factor for a $Gd_2O_2S:Tb$ phosphor screen employed in X-ray conventional and digital mammography. The curves were determined by Monte Carlo methods.

3.3. Experimental Techniques

In the following, we describe experimental methods focusing on techniques employed in our laboratory. In the experiments, the scintillators samples are used either as single crystals or as granular screens prepared by sedimentation of phosphor powders on suitable substrates. In both cases, the samples are irradiated by radiation from various sources (e.g., X-rays from mammographic and radiographic tubes as well as from therapeutic linear accelerators) at various energies (from 20 kV to some MVs). Absolute efficiency is

determined by measuring the light energy fluence emitted by the irradiated scintillator or phosphor (screen or single-crystal) and dividing by the incident exposure rate measured at the scintillator position. For the particular measurements, the crystal (or screen) is placed at a distance of 72.5 cm from the source. The emitted light fluence is determined by a photomultiplier tube coupled to the scintillator by an integrating sphere (EMI 9798 EMI Electronics LTD, Middlesex, UK and Oriel 70,451 Newport Co., Irvine, CA, USA, respectively). The current is measured by a femtoampere meter (Keithley 6430, Tektronix Inc., Beaverton, OR, USA). Exposure is measured by a dosimeter (RTI Piranha P100B, RTI Group, Mölndal, Sweden) located at the same distance. AE is then determined by dividing the current with the irradiated surface S , the sensitivity of the photocathode n_p , the spectral matching a_s between the photocathode and the light spectrum, the geometric light collection efficiency c_g for the light captured by the photocathode, and the exposure X as follows:

$$AE = \frac{\Psi_{\Lambda}}{X} = \left(\frac{i_{elec}}{S n_p a_s c_g} \right) X^{-1} \quad (22)$$

These measurements are performed for various radiation energies. To evaluate LE as a fraction of incident energy converted into emitted light energy flux, the following conversion factor, giving the radiation energy fluence corresponding to the measured exposure, was employed:

$$\Psi/X = [(\bar{W}/e)/(\mu_{en}/\rho)_{air}] \quad (23)$$

where \bar{W} is the mean energy required to create an electron–ion pair in air and $(\mu_{en}(E)/\rho)_{air}$ is the total mass energy absorption coefficient for air.

The light emission spectrum is measured by irradiating crystals or screens by a UV excitation source (Vilber-Lourmat VL-215M, Vilber-Lourmat GmbH, Eberhardzell, Germany) instead of X-rays since the UV source is two orders of magnitude higher, thus eliminating statistical fluctuations. The UV lamp–scintillator distance is 15 cm with a 45° angle to the crystal’s surface. A fiber optic (1m length, Avantes FCB-UV-400-2, Avantes B.V., Apeldoorn, The Netherlands) transfers the emitted light from the crystal to a high-resolution spectrometer (Ocean Optics HR2000, Ocean Optics, Duiven, The Netherlands). Alternatively, the luminescence efficiency can be determined by performing measurements in reflection mode (measuring the light emitted by the irradiated scintillator surface) by positioning a photometer (Universal Photometer Hagner) over a scintillating screen at a slight inclination with respect to the X-ray incidence [36]. In another study, a fluorescence spectrometer (Ocean optics QE Pro, Ocean Optics, Duiven, The Netherlands) coupled by fiber optics to an integrating sphere was also employed to determine light yield [101].

The MTF and NPS are determined following techniques that are explicitly described in previous studies [41,75,98]. The measurements are performed by coupling screens to a CMOS optical sensor (Remote RadEye HR, Teledyne DALSA, Waterloo, ON, Canada) consisting of a 1200 × 1200 photodiode array with a 22.5 μm pixel pitch.

For the determination of the MTF, images of suitable test patterns are obtained. Such patterns are the square wave response function (SWRF) pattern containing lead lines (e.g., the typ-53 of Nuclear Associates, Warrington, UK) and using Coltman’s formula, or a tungsten edge test device (PTW L659136, PTW, Freiburg, Germany), following the procedures described in the IEC standard [98].

The NPS can be experimentally determined following IEC 62220-1-2 and IEC 62220-1-1:2015 [98], i.e., by the Fourier transform (FT) of a large area flat field image $I(x_i, y_j)$ subtracted by a second-order polynomial fit \bar{I} in order to remove low-frequency background trends due to nonuniformities. This flat field image is separated into M regions of interest (ROIs) of 256 × 256 pixels half-overlapping with each other. Then, the NPS is expressed as:

$$NPS(u, v) = \frac{\Delta\chi\Delta y}{MN_x N_y} \sum_{m=1}^M \left| \sum_{i=1}^{N_x} \sum_{j=1}^{N_y} (I(x_i, y_j) - \bar{I}(x_i, y_j)) \exp(-2\pi i(u_n x_i + v_k y_j)) \right|^2 \quad (24)$$

where Δx and Δy are the pixel pitches in the x - and y -directions, N_x and N_y are dimensions of a region of interest (ROI) in the image, $I(x_i, y_i)$ is the flat field image for subROI i as a function of x and y , and $S(x_i, y_i)$ is a second-order polynomial fit according to the IEC standard. In addition to the *NPS*, the normalized noise power spectrum (*NNPS*) is usually employed to compare the noise features of different imaging systems. The *NNPS* is defined by:

$$NNPS(v) = \frac{NPS(v)}{\bar{\mu}^2} \quad (25)$$

where $\bar{\mu}^2$ is the square of the mean pixel value. *DQE* can be experimentally estimated according to IEC standard following the relation:

$$DQE(v) = \frac{MTF^2 NPS(v)}{K_a q NNPS(v)} \quad (26)$$

where q is the number of photons per unit kerma (μGy) per mm^2 , determined by dividing the number of photons per mm^2 (measured with a portable Amptek XR-100T X-ray spectrometer based on a cadmium telluride (CdTe) crystal) with the corresponding air kerma (K_a) value (μGy).

A variety of studies determining the MTF, NPS, and *DQE* of complete phosphor- and scintillator-based imaging systems have been published following similar techniques [101–103] or employing phantoms simulating anatomical structures [104], as well as techniques to determine the depth-dependent MTF within a scintillating screen [81].

4. Summary and Conclusions

In the present article, the use of scintillators and phosphors in medical imaging systems is presented by discussing the physical properties, the theoretical frameworks, and the image quality metrics as well as the corresponding experimental techniques. The imaging performance of scintillators and phosphors can be fully analyzed with theories based on light photon propagation either through scattering media or through optically transparent blocks. Biomedical imaging systems fall into two major medical fields, namely, diagnostic radiology and nuclear medicine. In projective diagnostic radiology, granular phosphors and structured crystals are used, while in nuclear medicine, they are mainly used in single crystalline form. Single crystals or ceramic scintillators are used in X-ray computed tomography. Detector systems may be either energy-integrating or photon-counting with spectrometric properties, mainly in nuclear medicine. Metrics for image quality evaluation have been defined based on such theories, i.e., the luminescence efficiency, MTF, NPS and *DQE*. Robust and well-established experimental techniques for the accurate determination of various performance parameters have been developed. As it can be observed from experimental data, only a small fraction of the incident radiation energy is converted into a useful signal (light), ranging approximately from 0.001 to 0.013. Thus, it may be concluded that phosphors and scintillators are not very efficient energy converters. This trend is favored in the complete imaging system as the signal (energy) propagates through several stages of signal conversion exhibiting signal losses. On the other hand, it should be emphasized that this trend exists; however, it is not of similar importance in the case of the signal-to-noise ratio (*DQE*), which is crucial for medical diagnosis. *DQE* decreases at a lower rate, i.e., 0.1–0.6.

Author Contributions: Conceptualization, I.K.; methodology, C.M. and I.K.; software, P.L. and C.M.; validation, C.M., N.K. and I.V.; formal analysis, I.K.; investigation, I.K., C.M. and N.K.; resources, G.F.; data curation, C.M.; writing—original draft preparation, I.K., C.M., P.L., N.K., I.V. and G.F.; writing—review and editing, I.K., C.M., P.L., N.K., I.V. and G.F.; visualization, I.K.; supervision, I.K.; project administration, I.K. All authors have read and agreed to the published version of the manuscript.

Funding: This research received no external funding.

Data Availability Statement: The original contributions presented in this study are included in this article. Further inquiries can be directed to the corresponding author/s.

Conflicts of Interest: The authors declare no conflicts of interest.

References

1. Blasse, G. The Luminescence Efficiency of Scintillators for Several Applications: State-of-the-Art. *J. Lumin.* **1994**, *60–61*, 930–935. [[CrossRef](#)]
2. Yaffe, M.J.; Rowlands, J.A. X-ray Detectors for Digital Radiography. *Phys. Med. Biol.* **1997**, *42*, 1. [[CrossRef](#)]
3. Moy, J.-P. Recent Developments in X-ray Imaging Detectors. *Nucl. Instrum. Methods Phys. Res. Sect. A Accel. Spectrometers Detect. Assoc. Equip.* **2000**, *442*, 26–37. [[CrossRef](#)]
4. Eijk, C.W.E. van Inorganic Scintillators in Medical Imaging. *Phys. Med. Biol.* **2002**, *47*, R85–R106. [[CrossRef](#)]
5. Nikl, M. Scintillation Detectors for X-rays. *Meas. Sci. Technol.* **2006**, *17*, R37–R54. [[CrossRef](#)]
6. Kandarakis, I.S. Luminescence in Medical Image Science. *J. Lumin.* **2016**, *169*, 553–558. [[CrossRef](#)]
7. Rowlands, J.A. The Physics of Computed Radiography. *Phys. Med. Biol.* **2002**, *47*, R123. [[CrossRef](#)] [[PubMed](#)]
8. Gruner, S.M.; Tate, M.W.; Eikenberry, E.F. Charge-Coupled Device Area X-ray Detectors. *Rev. Sci. Instrum.* **2002**, *73*, 2815–2842. [[CrossRef](#)]
9. Hoheisel, M. Review of Medical Imaging with Emphasis on X-ray Detectors. *Nucl. Instrum. Methods Phys. Res. Sect. A Accel. Spectrometers Detect. Assoc. Equip.* **2006**, *563*, 215–224. [[CrossRef](#)]
10. Milbrath, B.D.; Peurrung, A.J.; Bliss, M.; Weber, W.J. Radiation Detector Materials: An Overview. *J. Mater. Res.* **2008**, *23*, 2561–2581. [[CrossRef](#)]
11. Kubrin, R. Nanophosphor Coatings: Technology and Applications, Opportunities and Challenges. *KONA Powder Part. J.* **2014**, *31*, 22–52. [[CrossRef](#)]
12. Ronda, C.; Wiczorek, H.; Khanin, V.; Rodnyi, P. Review—Scintillators for Medical Imaging: A Tutorial Overview. *ECS J. Solid State Sci. Technol.* **2015**, *5*, R3121. [[CrossRef](#)]
13. Luo, Z.; Moch, G.J.; Johnson, S.S.; Chen, C.C. A Review on X-ray Detection Using Nanomaterials. *Curr. Nanosci.* **2017**, *13*, 364–372. [[CrossRef](#)]
14. Yanagida, T. Inorganic Scintillating Materials and Scintillation Detectors. *Proc. Jpn. Acad. Ser. B Phys. Biol. Sci.* **2018**, *94*, 75–97. [[CrossRef](#)] [[PubMed](#)]
15. Min, S.; Kang, H.; Seo, B.; Cheong, J.; Roh, C.; Hong, S. A Review of Nanomaterial Based Scintillators. *Energies* **2021**, *14*, 7701. [[CrossRef](#)]
16. Yanagida, T.; Kato, T.; Nakauchi, D.; Kawaguchi, N. Fundamental Aspects, Recent Progress and Future Prospects of Inorganic Scintillators. *Jpn. J. Appl. Phys.* **2022**, *62*, 010508. [[CrossRef](#)]
17. Rowlands, J.A.; Neitzel, U. Receptors for Projection Radiography. In *Diagnostic Radiology Physics: A Handbook for Teachers and Students*; Christofides, S., Dance, D.R., Maidment, A.D.A., McLean, I.D., Ng, K.-H., Eds.; International Atomic Energy Agency: Vienna, Austria, 2014; pp. 145–182.
18. Baily, D.L.; Humm, J.L.; Todd-Pokropek, A.; van Eijk, C.W.E. (Eds.) Basic Radiation Detectors. In *Nuclear Medicine Physics: A Handbook for Teachers and Students*; STI/PUB; International Atomic Energy Agency: Vienna, Austria, 2014; pp. 196–213. ISBN 978-92-0-143810-2.
19. Rowlands, J.A.; Yorkston, J. Flat Panel Detectors for Digital Radiography. In *Handbook of Medical Imaging Physics and Psychophysics*; Beutel, J., Kundel, H., Van Metter, R., Eds.; SPIE: Bellingham, WA, USA, 2000; Volume 1, pp. 223–328. ISBN 978-0-8194-7772-9.
20. Cherry, S.R.; Sorenson, J.A.; Phelps, M.E. *Physics in Nuclear Medicine*, 4th ed.; Elsevier/Saunders: Philadelphia, PA, USA, 2012.
21. Lecomte, R. Biomedical Imaging: SPECT and PET. *AIP Conf. Proc.* **2007**, *958*, 115–122. [[CrossRef](#)]
22. Boone, J.M. X-ray Production, Interaction, and Detection in Diagnostic Imaging. In *Handbook of Medical Imaging. Volume 1: Physics and Psychophysics*; Beutel, J., Kundel, H.L., Van Metter, R.L., Eds.; SPIE Press Book: Bellingham, WA, USA, 2000; Volume 1, pp. 1–79, ISBN 978-0-8194-7772-9.
23. Poletti, J.L. Projection Radiography. In *Diagnostic Radiology Physics: A Handbook for Teachers and Students*; Christofides, S., Dance, D.R., Maidment, A.D.A., McLean, I.D., Ng, K.-H., Eds.; International Atomic Energy Agency: Vienna, Austria, 2014; pp. 117–144.
24. Taibi, A. Conventional Radiology. In *Ionizing Radiation Detectors for Medical Imaging*; World Scientific: Singapore, 2004; pp. 17–52, ISBN 978-981-238-674-8.
25. Russo, P. Detectors for Digital Radiography. In *Ionizing Radiation Detectors for Medical Imaging*; World Scientific: Singapore, 2004; pp. 53–124. ISBN 978-981-238-674-8.
26. Passeri, A.; Formiconi, A.R. SPECT and Planar Imaging in Nuclear Medicine. In *Ionizing Radiation Detectors for Medical Imaging*; World Scientific: Singapore, 2004; pp. 235–285. ISBN 978-981-238-674-8.
27. Del Guerra, A.; Motta, A. Positron Emission Tomography. In *Ionizing Radiation Detectors for Medical Imaging*; World Scientific: Singapore, 2004; pp. 287–358. ISBN 978-981-238-674-8.
28. Ou, X.; Chen, X.; Xu, X.; Xie, L.; Chen, X.; Hong, Z.; Bai, H.; Liu, X.; Chen, Q.; Li, L.; et al. Recent Development in X-ray Imaging Technology: Future and Challenges. *Research* **2021**, *2021*, 9892152. [[CrossRef](#)] [[PubMed](#)]

29. Lu, L.; Sun, M.; Lu, Q.; Wu, T.; Huang, B. High Energy X-ray Radiation Sensitive Scintillating Materials for Medical Imaging, Cancer Diagnosis and Therapy. *Nano Energy* **2020**, *79*, 105437. [[CrossRef](#)]
30. Danielsson, M.; Persson, M.; Sjölin, M. Photon-Counting X-ray Detectors for CT. *Phys. Med. Biol.* **2021**, *66*, 03TR01. [[CrossRef](#)]
31. Lecoq, P. Development of New Scintillators for Medical Applications. *Nucl. Instrum. Methods Phys. Res. Sect. A Accel. Spectrometers Detect. Assoc. Equip.* **2016**, *809*, 130–139. [[CrossRef](#)]
32. Tyrrell, G.C. Phosphors and Scintillators in Radiation Imaging Detectors. *Nucl. Instrum. Methods Phys. Res. Sect. A Accel. Spectrometers Detect. Assoc. Equip.* **2005**, *546*, 180–187. [[CrossRef](#)]
33. Antonuk, L.E. Electronic Portal Imaging Devices: A Review and Historical Perspective of Contemporary Technologies and Research. *Phys. Med. Biol.* **2002**, *47*, R31. [[CrossRef](#)]
34. Jana, A.; Cho, S.; Patil, S.A.; Meena, A.; Jo, Y.; Sree, V.G.; Park, Y.; Kim, H.; Im, H.; Taylor, R.A. Perovskite: Scintillators, Direct Detectors, and X-ray Imagers. *Mater. Today* **2022**, *55*, 110–136. [[CrossRef](#)]
35. Gupta, S.K.; Mao, Y. Recent Advances, Challenges, and Opportunities of Inorganic Nanoscintillators. *Front. Optoelectron.* **2020**, *13*, 156–187. [[CrossRef](#)] [[PubMed](#)]
36. Lindström, J.; Alm Carlsson, G.; Wåhlin, E.; Carlsson Tedgren, Å.; Poludniowski, G. Experimental Assessment of a Phosphor Model for Estimating the Relative Extrinsic Efficiency in Radioluminescent Detectors. *Phys. Medica* **2020**, *76*, 117–124. [[CrossRef](#)] [[PubMed](#)]
37. Bohndiek, S.E.; Cook, E.J.; Arvanitis, C.D.; Olivo, A.; Royle, G.J.; Clark, A.T.; Prydderch, M.L.; Turchetta, R.; Speller, R.D. A CMOS Active Pixel Sensor System for Laboratory- Based X-ray Diffraction Studies of Biological Tissue. *Phys. Med. Biol.* **2008**, *53*, 655–672. [[CrossRef](#)]
38. Konstantinidis, A.C.; Szafraniec, M.B.; Speller, R.D.; Olivo, A. The Dexela 2923 CMOS X-ray Detector: A Flat Panel Detector Based on CMOS Active Pixel Sensors for Medical Imaging Applications. *Nucl. Instrum. Methods Phys. Res. Sect. A Accel. Spectrometers Detect. Assoc. Equip.* **2012**, *689*, 12–21. [[CrossRef](#)]
39. Yorkston, J. Recent Developments in Digital Radiography Detectors. *Nucl. Instrum. Methods Phys. Res. Sect. A Accel. Spectrometers Detect. Assoc. Equip.* **2007**, *580*, 974–985. [[CrossRef](#)]
40. Rocha, J.G.; Lanceros-Mendez, S. Review on X-ray Detectors Based on Scintillators and CMOS Technology. *Recent Pat. Electr. Eng.* **2011**, *4*, 16–41. [[CrossRef](#)]
41. Kim, H.-K.; Cunningham, I.A.; Yin, Z.; Cho, G.-S. On the Development of Digital Radiography Detectors: A Review. *Int. J. Precis. Eng. Manuf.* **2008**, *9*, 86–100.
42. Cowen, A.R.; Kengyelics, S.M.; Davies, A.G. Solid-State, Flat-Panel, Digital Radiography Detectors and Their Physical Imaging Characteristics. *Clin. Radiol.* **2008**, *63*, 487–498. [[CrossRef](#)]
43. Miller, S.R.; Gaysinskiy, V.; Shestakova, I.; Nagarkar, V.V. Recent Advances in Columnar CsI(Tl) Scintillator Screens. In Proceedings of the Penetrating Radiation Systems and Applications VII, San Diego, CA, USA, 1–4 August 2005; SPIE: Bellingham, WA, USA, 2005; Volume 5923, pp. 99–108.
44. Rocha, J.G.; Dias, R.A.; Goncalves, L.; Minas, G.; Ferreira, A.; Costa, C.M.; Lanceros-Mendez, S. X-ray Image Detector Based on Light Guides and Scintillators. *IEEE Sens. J.* **2009**, *9*, 1154–1159. [[CrossRef](#)]
45. Martinazzoli, L.; Kratochwil, N.; Gundacker, S.; Auffray, E. Scintillation Properties and Timing Performance of State-of-the-Art Gd₃Al₂Ga₃O₁₂ Single Crystals. *Nucl. Instrum. Methods Phys. Res. Sect. A Accel. Spectrometers Detect. Assoc. Equip.* **2021**, *1000*, 165231. [[CrossRef](#)]
46. Shefer, E.; Altman, A.; Behling, R.; Goshen, R.; Gregorian, L.; Roterman, Y.; Uman, I.; Wainer, N.; Yagil, Y.; Zarchin, O. State of the Art of CT Detectors and Sources: A Literature Review. *Curr. Radiol. Rep.* **2013**, *1*, 76–91. [[CrossRef](#)]
47. Makek, M.; Bosnar, D.; Kožuljević, A.M.; Pavelić, L. Investigation of GaGG:Ce with TOFPET2 ASIC Readout for Applications in Gamma Imaging Systems. *Crystals* **2020**, *10*, 1073. [[CrossRef](#)]
48. Xie, S.; Zhang, X.; Zhang, Y.; Ying, G.; Huang, Q.; Xu, J.; Peng, Q. Evaluation of Various Scintillator Materials in Radiation Detector Design for Positron Emission Tomography (PET). *Crystals* **2020**, *10*, 869. [[CrossRef](#)]
49. Yu, X.; Zhang, X.; Zhang, H.; Peng, H.; Ren, Q.; Xu, J.; Peng, Q.; Xie, S. Requirements of Scintillation Crystals with the Development of PET Scanners. *Crystals* **2022**, *12*, 1302. [[CrossRef](#)]
50. Zatcepin, A.; Ziegler, S.I. Detectors in Positron Emission Tomography. *Z. Für Med. Phys.* **2023**, *33*, 4–12. [[CrossRef](#)]
51. Zhu, D.; Nikl, M.; Chewpraditkul, W.; Li, J. Development and Prospects of Garnet Ceramic Scintillators: A Review. *J. Adv. Ceram.* **2022**, *11*, 1825–1848. [[CrossRef](#)]
52. Nikl, M.; Yoshikawa, A. Recent R&D Trends in Inorganic Single-Crystal Scintillator Materials for Radiation Detection. *Adv. Opt. Mater.* **2015**, *3*, 463–481. [[CrossRef](#)]
53. Zhang, H.; Wang, F.; Lu, Y.; Sun, Q.; Xu, Y.; Zhang, B.-B.; Jie, W.; Kanatzidis, M.G. High-Sensitivity X-ray Detectors Based on Solution-Grown Caesium Lead Bromide Single Crystals. *J. Mater. Chem. C* **2020**, *8*, 1248–1256. [[CrossRef](#)]
54. Tyagi, M.; Rawat, S.; Kumar, G.A.; Gadkari, S.C. A Novel Versatile Phoswich Detector Consisting of Single Crystal Scintillators. *Nucl. Instrum. Methods Phys. Res. Sect. A Accel. Spectrometers Detect. Assoc. Equip.* **2020**, *951*, 162982. [[CrossRef](#)]
55. Jin, T.; Hao, S.; Shang, Y.; Lei, Z.; Yang, C. Recent Trends in Elpasolite Single Crystal Scintillators for Radiation Detection. *Crystals* **2022**, *12*, 887. [[CrossRef](#)]
56. Piotrowski, W.M.; Bolek, P.; Brik, M.G.; Zych, E.; Marciniak, L. Frontiers of Deep-Red Emission of Mn⁴⁺ Ions with Ruddlesden–Popper Perovskites. *Inorg. Chem.* **2023**, *62*, 21164–21172. [[CrossRef](#)]

57. Bartosiewicz, K.; Fritz, V.; der Heggen, D.V.; Szymanski, D.; Zeler, J.; Pejchal, J.; Yamaji, A.; Kucerkova, R.; Beitlerova, A.; Kurosawa, S.; et al. Towards Deliberate Design of Persistent Phosphors: A Study of La–Ga Admixing in LuAG:Ce Crystals to Engineer Elemental Homogeneity and Carrier Trap Depths. *J. Mater. Chem. C* **2023**, *11*, 8850–8865. [CrossRef]
58. Elzbieciak-Piecka, K.; Sójka, M.; Tian, F.; Li, J.; Zych, E.; Marciniak, L. The Comparison of the Thermometric Performance of Optical Ceramics, Microcrystals and Nanocrystals of Cr³⁺ Doped Gd₃Ga₅O₁₂ Garnets. *J. Alloys Compd.* **2023**, *963*, 171284. [CrossRef]
59. Vedantham, S.; Karellas, A. Modeling the Performance Characteristics of Computed Radiography (CR) Systems. *IEEE Trans. Med. Imaging* **2010**, *29*, 790–806. [CrossRef]
60. Leblans, P.; Vandenbroucke, D.; Willems, P. Storage Phosphors for Medical Imaging. *Materials* **2011**, *4*, 1034–1086. [CrossRef] [PubMed]
61. Rivetti, S.; Lanconelli, N.; Bertolini, M.; Nitrosi, A.; Burani, A.; Acchiappati, D. Comparison of Different Computed Radiography Systems: Physical Characterization and Contrast Detail Analysis. *Med. Phys.* **2010**, *37*, 440–448. [CrossRef]
62. Sójka, M.; Piotrowski, W.; Marciniak, L.; Zych, E. Co-Doping to Extend the Operating Range of Luminescence Thermometers. The Case of Y₂SiO₅:Pr³⁺, Tb³⁺. *J. Alloys Compd.* **2024**, *970*, 172662. [CrossRef]
63. Xu, L.-J.; Lin, X.; He, Q.; Worku, M.; Ma, B. Highly Efficient Eco-Friendly X-ray Scintillators Based on an Organic Manganese Halide. *Nat. Commun.* **2020**, *11*, 4329. [CrossRef]
64. Blakesley, J.C.; Speller, R. Modeling the Imaging Performance of Prototype Organic X-ray Imagers. *Med. Phys.* **2008**, *35*, 225–239. [CrossRef]
65. Shao, W.; Zhu, G.; Wang, X.; Zhang, Z.; Lv, H.; Deng, W.; Zhang, X.; Liang, H. Highly Efficient, Flexible, and Eco-Friendly Manganese(II) Halide Nanocrystal Membrane with Low Light Scattering for High-Resolution X-ray Imaging. *ACS Appl. Mater. Interfaces* **2023**, *15*, 932–941. [CrossRef]
66. Chen, M.; Sun, L.; Ou, X.; Yang, H.; Liu, X.; Dong, H.; Hu, W.; Duan, X. Organic Semiconductor Single Crystals for X-ray Imaging. *Adv. Mater.* **2021**, *33*, 2104749. [CrossRef]
67. Rodnyi, P.A. *Physical Processes in Inorganic Scintillators*; CRC Press: London, UK, 2020; ISBN 978-0-13-874335-2.
68. Blasse, G.; Grabmaier, B.C. *Luminescent Materials*; Springer: Berlin/Heidelberg, Germany, 1994; ISBN 978-3-540-58019-5.
69. Bunch, P.C.; Huff, K.E.; Metter, R.V. Analysis of the Detective Quantum Efficiency of a Radiographic Screen–Film Combination. *J. Opt. Soc. Am. A* **1987**, *4*, 902–909. [CrossRef]
70. Ludwig, G.W. X-ray Efficiency of Powder Phosphors. *J. Electrochem. Soc.* **1971**, *118*, 1152. [CrossRef]
71. Nishikawa, R.M.; Yaffe, M.J. Model of the Spatial-Frequency-Dependent Detective Quantum Efficiency of Phosphor Screens. *Med. Phys.* **1990**, *17*, 894–904. [CrossRef] [PubMed]
72. Rabbani, M.; Shaw, R.; Metter, R.V. Detective Quantum Efficiency of Imaging Systems with Amplifying and Scattering Mechanisms. *J. Opt. Soc. Am. A* **1987**, *4*, 895–901. [CrossRef] [PubMed]
73. Cunningham, I.A. Applied Linear-Systems Theory. In *Handbook of Medical Imaging, Volume 1, Physics and Psychophysics*; Beutel, J., Kundel, H., Van Metter, R., Eds.; SPIE: Bellingham, WA, USA, 2000; Volume 1, pp. 79–156. ISBN 978-0-8194-7772-9.
74. Kim, H.K.; Yun, S.M.; Ko, J.S.; Cho, G.; Graeve, T. Cascade Modeling of Pixelated Scintillator Detectors for X-ray Imaging. *IEEE Trans. Nucl. Sci.* **2008**, *55*, 1357–1366. [CrossRef]
75. Zhao, C.; Kanicki, J.; Konstantinidis, A.C.; Patel, T. Large Area CMOS Active Pixel Sensor X-ray Imager for Digital Breast Tomosynthesis: Analysis, Modeling, and Characterization. *Med. Phys.* **2015**, *42*, 6294–6308. [CrossRef]
76. Swank, R.K. Calculation of Modulation Transfer Functions of X-ray Fluorescent Screens. *Appl. Opt. AO* **1973**, *12*, 1865–1870. [CrossRef] [PubMed]
77. Dobbins, J.T. Image Quality Metrics for Digital Systems. In *Handbook of Medical Imaging, Volume 1. Physics and Psychophysics*; Beutel, J., Kundel, H., Van Metter, R., Eds.; SPIE: Bellingham, WA, USA, 2000; pp. 161–223. [CrossRef]
78. Marshall, N.W. The Practical Application of Signal Detection Theory to Image Quality Assessment in X-ray Image Intensifier-TV Fluoroscopy. *Phys. Med. Biol.* **2001**, *46*, 1631. [CrossRef] [PubMed]
79. De Martinis, A.; Montalto, L.; Scalise, L.; Rinaldi, D.; Mengucci, P.; Michail, C.; Fountos, G.; Martini, N.; Koukou, V.; Valais, I.; et al. Luminescence and Structural Characterization of Gd₂O₂S Scintillators Doped with Tb³⁺, Ce³⁺, Pr³⁺ and F for Imaging Applications. *Crystals* **2022**, *12*, 854. [CrossRef]
80. Lubberts, G. Random Noise Produced by X-ray Fluorescent Screens. *J. Opt. Soc. Am.* **1968**, *58*, 1475–1483. [CrossRef]
81. Howansky, A.; Lubinsky, A.R.; Ghose, S.K.; Suzuki, K.; Zhao, W. Direct Measurement of Lubberts Effect in CsI:Tl Scintillators Using Single X-ray Photon Imaging. In Proceedings of the Medical Imaging 2017: Physics of Medical Imaging, Orlando, FL, USA, 13–16 February 2017; SPIE: Bellingham, WA, USA, 2017; Volume 10132, pp. 61–71.
82. Marshall, N.W. A Comparison between Objective and Subjective Image Quality Measurements for a Full Field Digital Mammography System. *Phys. Med. Biol.* **2006**, *51*, 2441. [CrossRef] [PubMed]
83. Nowotny, R. XMuDat: Photon Attenuation Data on PC, International Atomic Energy Agency. Available online: <https://www-nds.iaea.org/publications/iaea-nds/iaea-nds-0195.htm> (accessed on 31 March 2021).
84. Tseremoglou, S.; Michail, C.; Valais, I.; Ninos, K.; Bakas, A.; Kandarakis, I.; Fountos, G.; Kalyvas, N. Optical Photon Propagation Characteristics and Thickness Optimization of LaCl₃:Ce and LaBr₃:Ce Crystal Scintillators for Nuclear Medicine Imaging. *Crystals* **2024**, *14*, 24. [CrossRef]

85. Liaparinos, P.F. Optical Diffusion Performance of Nanophosphor-Based Materials for Use in Medical Imaging. *JBO* **2012**, *17*, 126013. [[CrossRef](#)] [[PubMed](#)]
86. Karpetas, G.E.; Michail, C.M.; Fountos, G.P.; Kalyvas, N.I.; Valais, I.G.; Kandarakis, I.S.; Panayiotakis, G.S. Detective Quantum Efficiency (DQE) in PET Scanners: A Simulation Study. *Appl. Radiat. Isot.* **2017**, *125*, 154–162. [[CrossRef](#)]
87. Cuplov, V.; Buvat, I.; Pain, F.; Jan, S. Extension of the GATE Monte-Carlo Simulation Package to Model Bioluminescence and Fluorescence Imaging. *JBO* **2014**, *19*, 026004. [[CrossRef](#)]
88. Zarrini-Monfared, Z.; Karbasi, S.; Zamani, A.; Mosleh-Shirazi, M.A. Full Modulation Transfer Functions of Thick Parallel- and Focused-Element Scintillator Arrays Obtained by a Monte Carlo Optical Transport Model. *Med. Phys.* **2023**, *50*, 3651–3660. [[CrossRef](#)]
89. Roncali, E.; Mosleh-Shirazi, M.A.; Badano, A. Modelling the Transport of Optical Photons in Scintillation Detectors for Diagnostic and Radiotherapy Imaging. *Phys. Med. Biol.* **2017**, *62*, R207. [[CrossRef](#)]
90. Liaparinos, P.F.; Kandarakis, I.S.; Cavouras, D.A.; Delis, H.B.; Panayiotakis, G.S. Modeling Granular Phosphor Screens by Monte Carlo Methods. *Med. Phys.* **2006**, *33*, 4502–4514. [[CrossRef](#)] [[PubMed](#)]
91. Dainty, J.C.; Shaw, R. *Image Science*; Academic Press: New York, NY, USA, 1974.
92. Siewerdsen, J.H.; Antonuk, L.E.; El-Mohri, Y.; Yorkston, J.; Huang, W.; Boudry, J.M.; Cunningham, I.A. Empirical and Theoretical Investigation of the Noise Performance of Indirect Detection, Active Matrix Flat-Panel Imagers (AMFPIs) for Diagnostic Radiology. *Med. Phys.* **1997**, *24*, 71–89. [[CrossRef](#)] [[PubMed](#)]
93. Yaffe, M.J.; Mainprize, J.G. Detectors for Digital Mammography. *Technol. Cancer Res. Treat* **2004**, *3*, 309–324. [[CrossRef](#)]
94. Yun, S.; Kim, S.H.; Kim, D.W.; Kim, H.K. Detective Quantum Efficiency of a Phosphor-Coupled Photodiode Array Detector for Use in Digital X-ray Tomosynthesis Systems. *NDT E Int.* **2017**, *92*, 130–135. [[CrossRef](#)]
95. Linardatos, D.; Konstantinidis, A.; Valais, I.; Ninos, K.; Kalyvas, N.; Bakas, A.; Kandarakis, I.; Fountos, G.; Michail, C. On the Optical Response of Tellurium Activated Zinc Selenide ZnSe:Te Single Crystal. *Crystals* **2020**, *10*, 961. [[CrossRef](#)]
96. Tseremoglou, S.; Michail, C.; Valais, I.; Ninos, K.; Bakas, A.; Kandarakis, I.; Fountos, G.; Kalyvas, N. Evaluation of Cerium-Doped Lanthanum Bromide (LaBr₃:Ce) Single-Crystal Scintillator's Luminescence Properties under X-ray Radiographic Conditions. *Appl. Sci.* **2023**, *13*, 419. [[CrossRef](#)]
97. Tseremoglou, S.; Michail, C.; Valais, I.; Ninos, K.; Bakas, A.; Kandarakis, I.; Fountos, G.; Kalyvas, N. Efficiency Properties of Cerium-Doped Lanthanum Chloride (LaCl₃:Ce) Single Crystal Scintillator under Radiographic X-ray Excitation. *Crystals* **2022**, *12*, 655. [[CrossRef](#)]
98. International Electrotechnical Commission International Electrotechnical Commission IEC 62220-1-1:2015 Medical Electrical Equipment: Characteristics of Digital X-ray Imaging Devices. Part 1-1. Available online: <https://webstore.iec.ch/publication/21937> (accessed on 7 January 2024).
99. Tzomakas, M.K.; Peppas, V.; Alexiou, A.; Karakatsanis, G.; Episkopakis, A.; Michail, C.; Valais, I.; Fountos, G.; Kalyvas, N.; Kandarakis, I.S. A Phantom Based Evaluation of the Clinical Imaging Performance of Electronic Portal Imaging Devices. *Heliyon* **2023**, *9*, e21116. [[CrossRef](#)]
100. Michail, C.M.; Fountos, G.P.; Liaparinos, P.F.; Kalyvas, N.E.; Valais, I.; Kandarakis, I.S.; Panayiotakis, G.S. Light Emission Efficiency and Imaging Performance of Gd₂O₂S:Eu Powder Scintillator under X-ray Radiography Conditions. *Med. Phys.* **2010**, *37*, 3694–3703. [[CrossRef](#)] [[PubMed](#)]
101. Zhu, W.; Ma, W.; Su, Y.; Chen, Z.; Chen, X.; Ma, Y.; Bai, L.; Xiao, W.; Liu, T.; Zhu, H.; et al. Low-Dose Real-Time X-ray Imaging with Nontoxic Double Perovskite Scintillators. *Light Sci. Appl.* **2020**, *9*, 112. [[CrossRef](#)] [[PubMed](#)]
102. Lu, X.; Zhang, J. The Measurement and Evaluation of Standard DQE in Digital Radiography. In Proceedings of the 2015 International Conference on Mechatronics, Electronic, Industrial and Control Engineering, Shenyang, China, 1–3 April 2015; Atlantis Press: Amsterdam, The Netherlands, 2015; pp. 9–12.
103. Rivetti, S.; Lanconelli, N.; Bertolini, M.; Nitrosi, A.; Burani, A. Characterization of a Clinical Unit for Digital Radiography Based on Irradiation Side Sampling Technology. *Med. Phys.* **2013**, *40*, 101902. [[CrossRef](#)] [[PubMed](#)]
104. Bertolini, M.; Nitrosi, A.; Rivetti, S.; Lanconelli, N.; Pattacini, P.; Ginocchi, V.; Iori, M. A Comparison of Digital Radiography Systems in Terms of Effective Detective Quantum Efficiency. *Med. Phys.* **2012**, *39*, 2617–2627. [[CrossRef](#)]

Disclaimer/Publisher's Note: The statements, opinions and data contained in all publications are solely those of the individual author(s) and contributor(s) and not of MDPI and/or the editor(s). MDPI and/or the editor(s) disclaim responsibility for any injury to people or property resulting from any ideas, methods, instructions or products referred to in the content.